GEOPHYSICS, VOL. 68, NO. 6 (NOVEMBER-DECEMBER 2003); P. 1922–1933, 15 FIGS.
10.1190/1.1635046

Propagation of a ground-penetrating radar (GPR) pulse in a thin-surface waveguide

Steven A. Arcone*, Paige R. Peapples‡, and Lanbo Liu**

ABSTRACT

Field observations are tested against modal propagation theory to find the practical limitations upon derivation of layer permittivities and signal attenuation rates from a radar moveout profile over two-layer ground. A 65-MHz GPR pulse was transmitted into a 30-60-cm-thick surface waveguide of wet, organic silty to gravelly soil overlying a drier refracting layer of sand and gravel. Reflection profiles, trench stratigraphy, resistivity measurements, and sediment analysis were used to quantify the propagation medium and possible attenuation mechanisms.

Highly dispersive modal propagation occurred within the waveguide through 35 m of observation. The fastest phase velocity occurred at the waveguide cutoff frequency of 30 MHz, which was well received by 100-MHz antennas. This speed provides the refractive index of the lower layer, so the near-cutoff frequencies must match a lower layer refraction. A slower, lower frequency phase of the dispersed pulse occurred at about 60–70 MHz, with an average attenuation rate of about 0.4 dB/m. Similar events appear to have reflected back and forth along the waveguide. Modal theory for the average layer thickness shows all primary events to be different aspects of a TE_1 mode, predicts the correct 30–70-MHz phase speeds and low-frequency cutoff phenomenon, but also predicts that the 60–70-MHz group speed should be slightly lower than observed. An Airy phase was apparently out of the bandwidth. Two-dimensional finite-difference time-domain modeling qualitatively simulates the main field results.

After accounting for an inverse dependency of amplitude on the square of the range, the high resistivity of the surface layer accounts for the 0.4-dB/m attenuation rate for the 60–70-MHz phase of the pulse. However, erratic amplitudes, interface roughness, and the reflected packets indicate scattering. We conclude that permittivities can be well estimated from dispersive moveout profiles given an average surface layer thickness, and the wide bandwidth of GPR antennas allows the full dispersion to be seen. Attenuation rates appear to be derivable from the higher frequency part of our dispersive event, for which attenuation might be least affected by the waveguide dispersion.

INTRODUCTION

Variable antenna offset profiles are used with ground-penetrating radar (GPR) surveys to interpret the dielectric permittivities of near-surface layers from measured wave velocities (Fisher et al., 1992; Annan et al., 1994). However, when the thickness of the surface layer compares with or is smaller than a wavelength in the material, modal and dispersive propagation occur in this layer at speeds that may not correspond with the actual layer permittivities. Only two cases permit propagation over more than about 10 m for most frequencies and two-layer ground of practical interest. The first is where the lower layer is a strong reflector—for example, water beneath ice, or clay or saturated sediment beneath dry sediment—and of relatively higher permittivity than the surface layer. In this case, the lowest (near-cutoff) frequency of a single, dispersive mode supports an air refraction and propagates at the air velocity (30 cm/ns), while a higher frequency indicative of an Airy phase propagates at a slower velocity that does not equal the intrinsic speed of the layer medium (Ewing et al., 1957; Arcone, 1984). The second case is when the lower layer has a relatively lower permittivity—for example, frozen or drier sediments beneath

Manuscript received by the Editor July 16, 2002; revised manuscript received April 4, 2003.
*Engineering Research and Development Center, U.S. Army Cold Regions Research and Engineering Laboratory, 72 Lyme Road, Hanover, New Hampshire 03755. E-mail: steven.a.arcone@eroc.usace.army.mil.
‡Formerly, ERDC, U.S. Army Cold Regions Research and Engineering Laboratory, Hanover, New Hampshire 03755; presently Alaskan State Geologic and Geophysical Surveys, 794 University Avenue, Suite 200, Fairbanks, Alaska 99709. E-mail: paige_peapples@dnr.state.ak.us.
**Formerly ERDC, U.S. Army Cold Regions Research and Engineering Laboratory, Hanover, New Hampshire 03755; presently University of Connecticut, Department of Geology and Geophysics, 354 Mansfield Road, U-2045, Storrs, Connecticut 06269-2045. E-mail: lanbo.liu@uconn.edu.

unfrozen or wetter sediments (Arcone et al., 1998)—which also supports a refraction. Propagation within such dispersive, or channel, structures is well known in seismology (Ewing et al., 1957; Grant and West, 1965).

We investigate radiowave dispersive modal propagation in a real refractive waveguide. Our interest in this problem arose from our need to interpret depths to a local water table from GPR surveys (Astley et al., 1999). Our objective was to find what constraints might be imposed upon the interpretation of intrinsic wave velocity and attenuation rates by the modal propagation and by the additional complications of the natural variability of waveguide thickness, as well as other practical considerations such as antenna bandwidth and impedance loading. Our approach was to test field observations against predictions of the classic, modal waveguide equation for single frequencies and of 2D finite-difference time-domain (FDTD) modeling of the pulse propagation dynamics. We used a GPR system and 100-MHz design frequency antennas to generate pulses, and we monitored them along the ground surface in standard moveout surveys. The slower speed waveguide consisted of wetter silt, sand, cobbles, and organics situated above a faster layer of drier sands, gravels, and cobbles within an alluvial deposit near Anchorage, Alaska. We determined the thickness, structure, and intrinsic radiowave speed of our layers with GPR reflection profiles, a trench, and a well log. We used field and laboratory measurements of the grain size, porosity, water content, formation resistivity, and rock permittivity to support our observations of dielectric, attenuation, and dispersive properties measured in the field. Generally, we precluded the use of network analyzer-based waveguide impedance measurements because of the coarse nature of the sediments and an inability to reproduce in-situ densities.

MODAL PROPAGATION THEORY

Modal propagation within a layer waveguide (of permittivity ε_2) refers to lossless propagation and is especially dispersive when the layer thickness is close to or less than an in-situ wavelength λ (Arcone, 1984; Arcone et al., 1998). In a two-layer dielectric ground, lossless (nonleaky) modes occur when the confining layers (e.g. air above, for which $\varepsilon_1 = 1$, and dry sand ε_3 below) have lower permittivities than the waveguide. In this case a refraction will occur in the lower layer at the critical angle, and dispersive modes will develop in the upper layer (Figure 1). Depending on waveguide thickness d and ε_2, higher order modes will develop which have phase fronts that propagate at speeds determined by discrete angles (measured from vertical) greater than the critical angle. The lowest order mode is always the strongest and most important. The modes are determined by the modal equation (Budden, 1961) for either transverse electric (TE) or transverse magnetic (TM) waves, such that

$$R_{01} R_{12} \exp(i 2 k_2 d \cos\theta) = 1, \qquad (1)$$

where R_{01} and R_{12} are the TE or TM reflection coefficients for the upper and lower layer interfaces, respectively; $k_2 = k_0\sqrt{\varepsilon_2}$

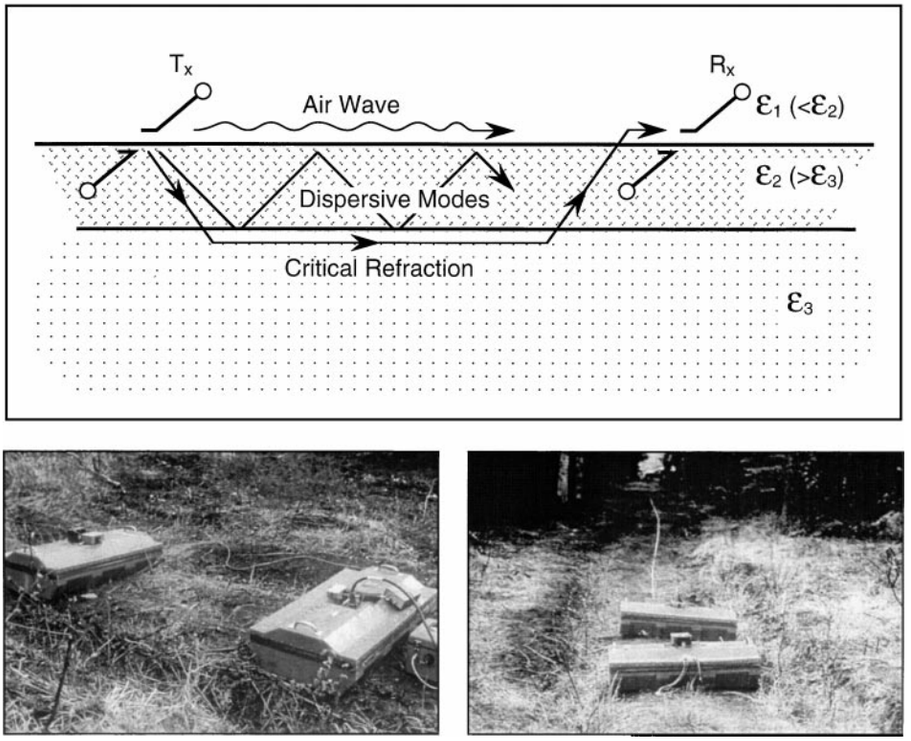

FIG. 1. (Top) Diagram of the transmit (Tx) and receive (Rx) antennas, airwave, waveguide dispersive modes, and refraction. At our study site, the drier and coarser sand, gravels, and cobbles have a lower relative dielectric permittivity (ε_3) and wave velocity than do the overlying wetter and finer grained sediments (ε_2). (Bottom) 100-MHz antennas with fiberoptic circuitry to trigger the receiver (left) and antennas on the study line (right).

is the propagation function for the refracting layer; and θ is the modal angle of a particular frequency with respect to vertical. The quantity $k_0 = 2\pi f/c$, where f is frequency in Hz and $c = 30$ cm/ns. The phase velocity of any particular frequency is

$$v_{ph} = \frac{c}{\sqrt{\varepsilon_2}\sin\theta}. \quad (2)$$

For our case of parallel and facing antennas, we consider only TE waves. In this case all modes have a minimal cutoff frequency where phase and group velocities equal the velocity within an adjacent, refracting layer and a higher frequency at which minimum group velocity occurs and energy is theoretically maximized. This latter phenomenon is known as the Airy phase (Ewing et al., 1957; Grant and West, 1965). For given values of d and the permittivities of each layer, several modes might exist, each of which can support all frequencies above their own particular cutoff frequency.

Modal propagation losses are caused by transmission through the waveguide interfaces, intrinsic attenuation within the medium itself, and geometric wavefront spreading. Interface transmission losses and intrinsic attenuation, such as caused by conduction currents or scattering, may be expressed through a complex, equivalent propagation angle $\theta + i\gamma$, for which the phase velocity then becomes

$$v_{ph} = \frac{c}{\sqrt{\varepsilon_2}\sin\theta\cosh\gamma}. \quad (3)$$

If $\varepsilon_3 > \varepsilon_2$, then transmission leakage into the lower layer can produce values of γ near unity and attenuation rates can approach several tens of decibels per meter. For the case of our refractive waveguide, however, real energy loss occurs strictly through medium attenuation mechanisms. Apparent energy loss at any particular frequency occurs from the dispersive process itself.

For geometric spreading losses we consider that the amplitudes of modes, refractions, and any kind of lateral surface wave decay in proportion to r^2, where r is the range separation between transmitter and receiver antennas. The range is both several wavelengths from the source and much greater than the surface layer depth. We assume this range dependency because very thin layers (in terms of λ) support nearly interfacial waves; interfacial waves along homogeneous ground follow this behavior (Annan, 1973), and so do seismic refractions (Heelan, 1953; O'Brien, 1967). Furthermore, the low-frequency wave velocity that developed in our surface waveguide emulates a refraction along the lower interface. Annan (1973) briefly discusses this point for very thin waveguides. In our waveguide, the average electrical thickness for $\varepsilon = 23$ was only 0.4λ (at 70 MHz), and the minimum measurement range was about 5λ.

EQUIPMENT AND FIELD METHODS

We used the Geophysical Survey Systems, Inc. (GSSI) model 10b control unit to set radar parameters and record data to hard disk. We used separate transmitter and receiver resistively loaded antennas with bandwidths nominally centered near dominant frequencies (DF, the inverse of the dominant period) of 100 (GSSI model 3207), 400 (model 5103), and 1200 (model 5100) MHz, the latter two being used for supplemental media characterization. However, the ground loading by the high-permittivity near-surface ground reduced the DF to about 65 MHz for model 3207 (Figure 2) and to about 280 MHz for model 5103. The peak powers for the 400- and 100-MHz transmitters are rated by the manufacturer at 1.2 and 800 W, respectively, but these values refer to the power absorbed by a 200-ohm resistor at the antenna terminals. The actual radiated power is probably less. The simplest form of the reflected wavelets lasts about $2^1/_2$ cycles (Figure 2), for which the central $1^1/_2$ cycles are strongest and better approximate the form of the original transmission. The 3-dB bandwidth of the $2^1/_2$-cycle wavelet is about 35% of the DF. This form depends slightly upon the time-dependent gain applied to the recording, which we removed for our attenuation analysis. The extra half to one cycle can be added by reverberation associated with a thin layer response or with a surface layer, as is our case here.

We continuously dragged all antennas for reflection profiles and recorded 16-bit samples per trace. Our processing included position normalization and band-pass filtering to reduce electronic and antenna-to-ground coupling noise. Very small corrections in the time scales of the reflection profiles were made to account for the antenna offsets, which were only 15 cm for model 5103 and 1.6 m for model 3207. We constructed the offset profiles by recording at 20-cm increments both north and south from the center of our study transect, which was located at a logged well. Contact between antenna and ground always appeared optimal, and the dipoles were always aligned within a few degrees of normal to the propagation direction; rotation of the receiver antenna always resulted in a decrease in peak signal amplitude. We stacked 128 traces to reduce noise, set our time range to 600 ns, and extended our antenna separations to 35 m. In retrospect, this range could have been greatly extended. We used the 1200-MHz antennas to obtain reflection profiles of individual, flat-sided boulders to determine rock permittivities from the time delays of bottom reflections and the measured thicknesses.

SITE DESCRIPTION

Our site is about 20 km north of Anchorage, Alaska, and just east of Fort Richardson near Ship Creek (Figure 3). We conducted our study along a 100-m section of a cleared line that included a gravel pit (Figure 4). The profile section is within valley outwash alluvium that appears to have incised a surrounding lateral moraine. Exposures along Ship Creek (Hunter et al., 2000) and within the gravel pit show stratification within the gravels. We identified the igneous and metamorphic clasts to be mainly granite, metagreywacke, and volcanics

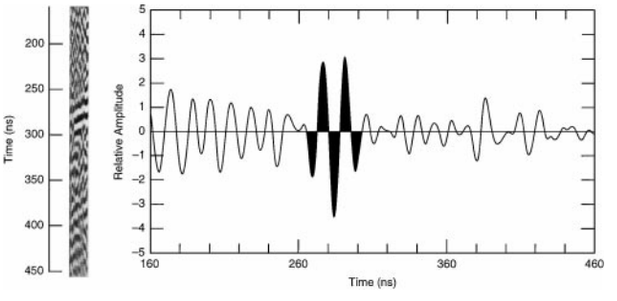

FIG. 2. Reflected form of the wavelet (shaded signal) and equivalent line intensity representation in a reflection profile. The DF of this wavelet is 65 MHz. The wavelet is the inverse of the transmitted wavelet because it is a subsurface reflection from a water table.

(probably andesite). The variability is consistent with the subduction melange character of the rock sources throughout the Matanuska and nearby Chugach Mountain valleys feeding into the Anchorage area (Winkler, 1992).

RESULTS

Layer properties

The stratification we observed to about 2.5 m depth in a trench beneath our study line showed two distinct layers (Figure 5). The surface layer thickness was 30–60 cm, averaged 34 cm with a standard deviation of 7 cm, and appeared to vary no more than about 5 cm over distances of about 100 cm. A sample of the near-surface sandy silt had a dry density of 1.43 gr cm^{-3}, and four samples of the organic sand and silt had an average volumetric water content of 0.29. We estimate the porosity to have been about 0.47. The second layer showed intermittent sections of laminations and more widely spaced strata within the upper portion (Figure 5). A 32-gallon barrel sediment sample gave a porosity of about 19% and an average volumetric water content of about 7–8% (four samples ranging from 0.047 to 0.103 with an average of 0.075). This porosity might be slightly high from our unpacking of the natural formation. The volumetric percentage of clasts greater than about 5 cm in maximum dimension in either layer was only 8%, with almost no cobbles greater than 10 cm. The CRIM mixing formula (Annan et al., 1994) (see the Appendix) gives $\varepsilon_2 = 10.7$, given that the average ε for the sediments is 9, as it is for the large boulders in the area (see Appendix). This value agrees almost exactly with that calculated from the reflection-time delay from the bottom of this layer, as discussed below.

A 1998 well log located at 0 m revealed a wet surface layer of cobbles, fine sand, silt, and organics and then a 10-m-thick layer of moist, sandy gravel, followed by a 6-m-thick layer of dry sand. The bottom of the sand contained a thin water table at 16 m depth that was perched on a silt- and clay-rich layer. Consistently, a logged borehole beneath the floor of the 4–5-m-deep gravel pit 300 m to the south showed a water table at 12 m depth.

Our reflection profiles are consistent with these observations. In the 280-MHz GPR profile (Figure 5), the white arrows indicate the reflection from the bottom of the surface layer. The average time delay to the bottom is 10.8 ns, which gives an $\varepsilon_2 = 23$ for the average depth of 34 cm. This time delay accounts for antenna separation and was measured to the leading edge of the reflected pulse. This permittivity value could range between 21 and 25 because the accuracy of the time picks was about +0.5 ns. The profile then reveals intermittent stratification within the second layer to a depth of about 4.5 m.

Our 65-MHz profile (Figure 6) does not resolve the surface layer but does show two sets of deep, intermittent reflections of variable time delays. At 0 m distance, the 217-ns time delay between the first and second reflection horizons and the 10-m borehole layer depth of the moist gravel give $\varepsilon_3 = 10.6$, which means this layer can support a refraction. The 106-ns time delay within the lower 6-m-thick dry layer gives $\varepsilon = 7.0$. The intermittent appearance of the water table suggests that water is confined to aquifers.

There are no hyperbolic diffractions originating beneath the surface layer within either reflection profile. Instead, there are diagonal streaks, which we interpret to be backscattered modes

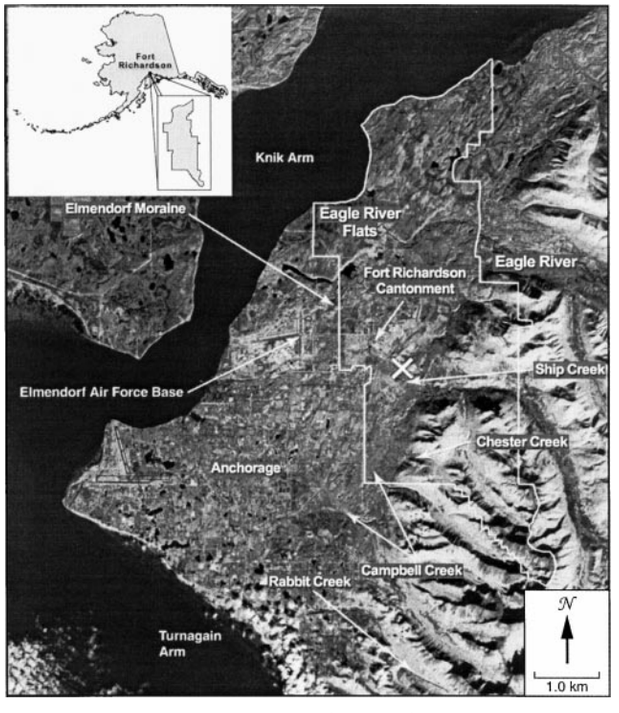

FIG. 3. Location of our study site (white ×) at Ship Creek, Fort Richardson, Alaska.

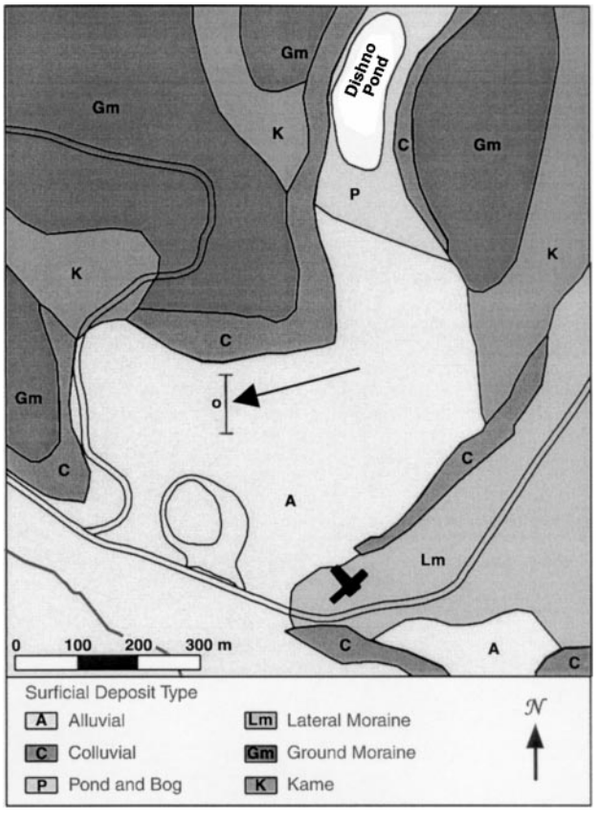

FIG. 4. Location of our study transect (arrow) within alluvial outwash (geology compiled by Astley et al., 1999). The circular area represents a gravel pit.

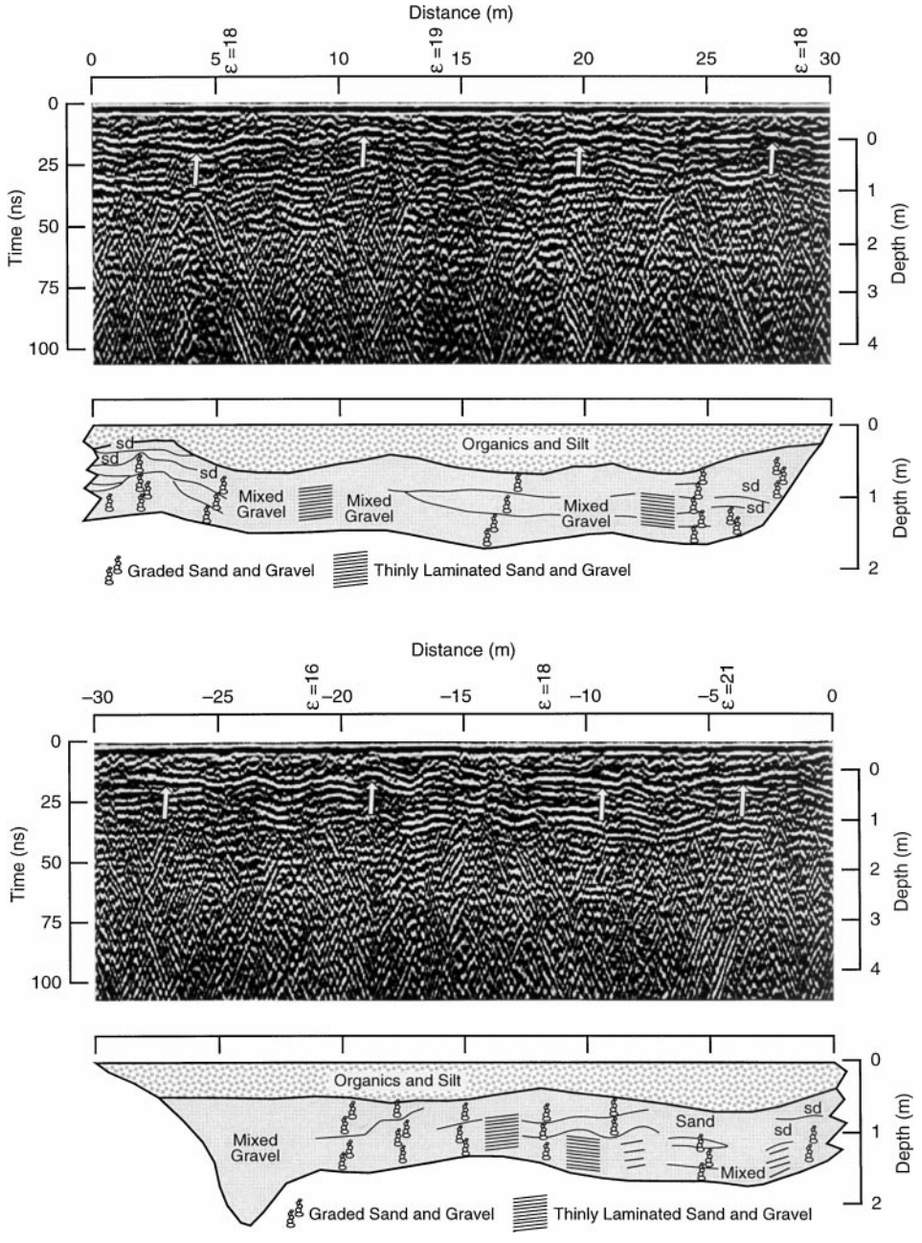

FIG. 5. Trench observations and corresponding 280-MHz reflection profiles. The depth scale of the profile begins beneath the surface layer. The borehole to the water table is located at 0 m. The ε values above the profiles were calculated from the slopes of the waveguide modes, which give group velocities.

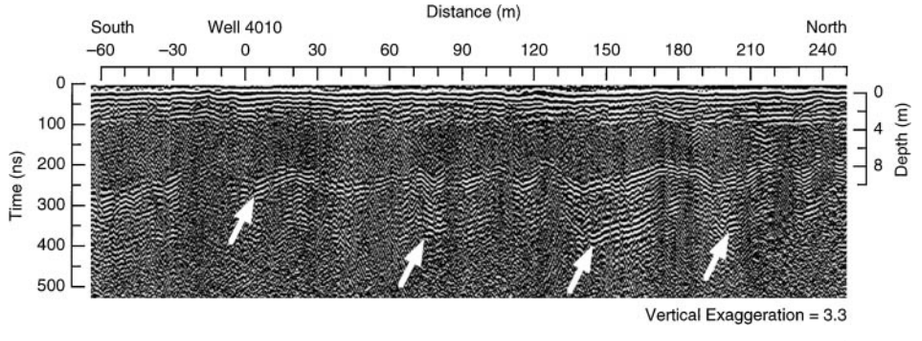

FIG. 6. The 65-MHz profile of our extended line, including our study section. The water table reflections (arrows at 70–80, 130–180, and 190–210 m) are intermittent. All arrows also indicate reflections where the DF is about 60–70 MHz (Figure 2).

in the surface layer. Their slopes in the 280-MHz profile show a group velocity effective ε of 16 to 21. Using the Complex Refractive Index Model mixing formula, assuming (1) the mineral sandy silt has the same average, $\varepsilon = 9$, as do the clasts (discussed later), and (2) the interstitial water has the same ε as does free water, the 0.29 average volumetric water content for this layer predicts $\varepsilon = 20$ (see Appendix). In the 65-MHz profile in Figure 6, the apexes of the streaks originate beneath the surface layer at 1 to 5 m depth, and their slopes correspond with an ε of about 20 (discussed later). Thus, they appear to be waveguide modes that were excited by diffractions.

We performed a Wenner dc resistivity (ρ) sounding centered between our refraction lines (Figure 7) in September 1998. The interpretation (Interpex software iterative, least-squares fitting model) gives the depth to the water table at 20 m and a moderately resistive surface layer of 20 cm thickness. This water table depth is too great by 25%, and the closest electrode spacing (1 m) and the depth of the probes (about 20 cm) were both too large to enable correct resolution of the surface layer. The important parameter, however, is the resistivity value of 885 ohm-m, which is surprisingly high in a view of the water content and high permittivity but is consistent with the wide variety of grain sizes. In August 2000 we corroborated these very near-surface values using a l-m probe spacing with small probes along the trench wall. Consistent with the 1998 readings, we found a section of organic silt to be at 1400 ohm-m and a section of purer silt at 2700 ohm-m, while repeat reflection surveys at 280 MHz still showed the surface layer to have an ε_2 of 23.

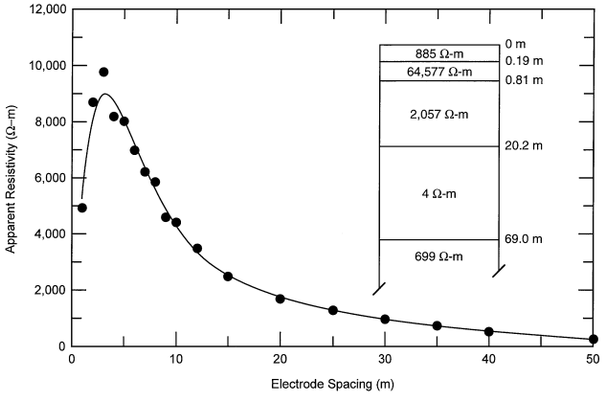

FIG. 7. Wenner dc resistivity sounding centered at 0 m and interpreted layer structure.

Offset profiles

Our wide-angle offset profiles, both recorded with the receiver fixed at 0 m (Figure 8), show similar modal behavior. The close agreement of our calculated airwave velocity (29.8 cm/ns) with the correct value of 30 cm/ns validates the system time range calibration. All events subsequent to the air waves appear to propagate as two wave packets, one at lower frequency and one at higher frequency. In this dispersion, lower and faster, followed by progressively higher and slower, frequency phase fronts propagate through the wave packet and die out at the front. All phase fronts exhibit shingling; leading phase fronts die out with increasing range while new, trailing ones emerge. Both profiles show a very slight decrease in slope in the lower frequency phase fronts as separation increases, which is consistent with normal dispersion. The first few cycles of these faster events begin to separate from the higher frequency propagation at about 10 m antenna separation. The DF of their leading $1\frac{1}{2}$ cycles is about 50 MHz near 10 m separation, progressively decreasing to about 30 MHz by 25 m separation (Figure 9). After about 10 m the slope of the 30–50-MHz phase fronts in Figure 8 remains fairly constant to give $\varepsilon = 10 \pm 0.7$, in agreement with our interpretation of the 65-MHz reflection profile time delay and well-log thickness for the upper gravel layer. The agreement between horizontally and vertically determined permittivity values shows that the refracting layer exhibits large-scale isotropy.

The DFs of the later arriving cycles at 15 to 25 m separation are centered between 60 and 70 MHz. Shingling is most apparent in this secondary packet, and their group velocity, estimated from the slope along the en echelon phase fronts, corresponds with an equivalent $\varepsilon \approx 30$. The slopes of the individual phase fronts give $\varepsilon = 15$. There are also 60–70-MHz events with positive slopes that emerge beneath the modes. We interpret these events to be multiple backscattered reflections within the waveguide. A close view reveals these are also shingled.

We used both time- and frequency-domain approaches to compute attenuation rates for the modal events of Figure 8. The frequency-domain analysis is questionable because the

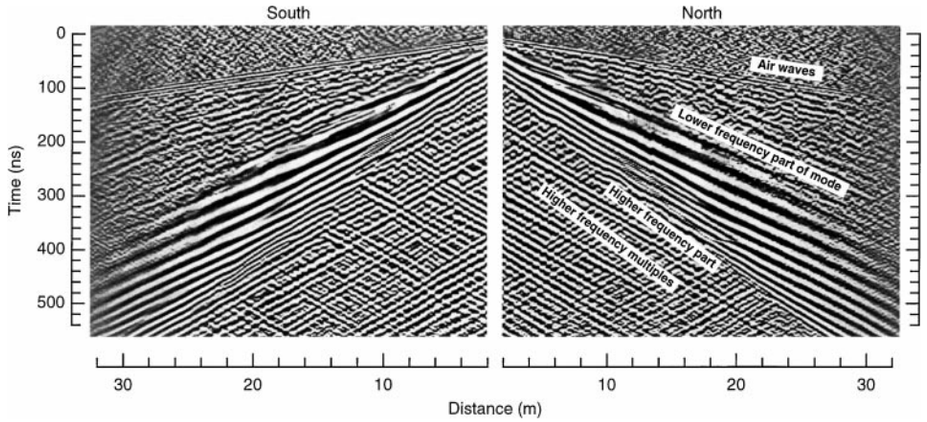

FIG. 8. Wide-angle moveout profiles extended north and south from the center of our study line. Automatic gain control has been applied to this profile to emphasize all events.

time-domain windowing used to eliminate the backward-propagating mode reflections produced discrete spectra for each trace that could not be interpreted. In the time domain we computed the average amplitude of three of the leading half-cycles of the 30–50-MHz portion of the waveform for both north and south profiles (Figure 10) and that of the amplitude envelope of the multicycle 60–70-MHz packet for the south profile (Figure 11); the packet on the north could not be evaluated consistently. We corrected for the square of the range and for the recorded range gain. Although the amplitudes vary considerably, a linear regression analysis for the three half-cycles of the 30- to 50-MHz portion of the waveforms gives an average rate of about 1.1 dB/m for the north profile and 1.5 dB/m for the south. The rms deviations from the straight-line fits are 1.0 dB for the north profile and 1.6 dB for the south. The R^2 correlation coefficients are 0.95 and 0.97 for the south and north profiles, respectively. In contrast, the average rate for the 60–70-MHz packet is only about 0.44 dB/m. The quantization errors for the 60–70-MHz packet prevent a fair analysis of the rms deviation from the straight-line fit. A one-bit error for the measurements beyond 23 m range would increase the rate to 1 dB/m, but this rate, as well as those measured for 30–50-MHz cycles, are too high to be consistent with loss rates predicted by the measured resistivities for the upper layer, as discussed below.

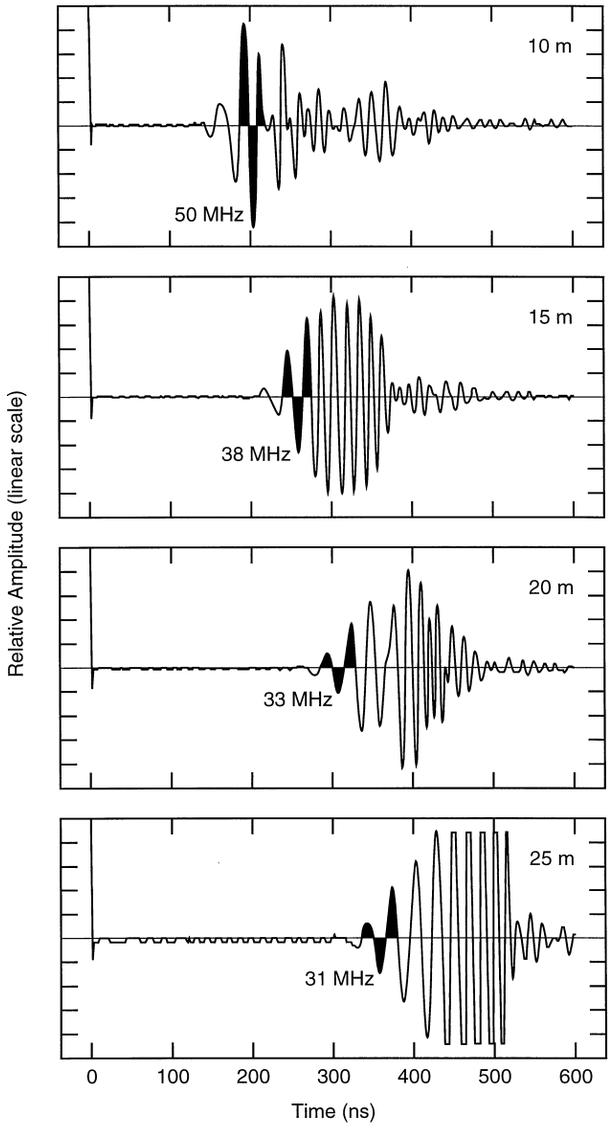

FIG. 9. Sample traces at various antenna separations within the south-side moveout profile. The DF is labeled beneath the leading cycles (shaded) analyzed. The lower three traces also show the 60–70-MHz packet analyzed for attenuation rate. The trace at 25 m has been amplified 4×.

DISCUSSION

Application of modal propagation theory

We interpret all forward propagating events as parts of one dispersive, lowest order TE mode, with the faster events appearing as an apparent refraction because they propagate at the intrinsic speed of the second layer. Equation (1) supports several aspects of the offset propagation. Figure 12 shows that

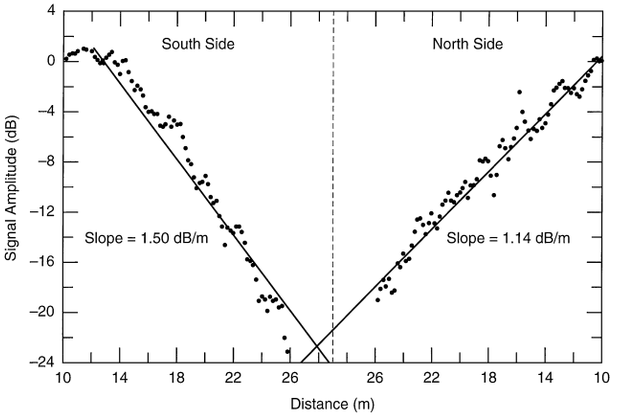

FIG. 10. Average amplitudes of the leading three half-cycles of the refracted wavelets as a function of antenna separation. The amplitudes have been corrected for the applied range gain and the square of the separation distance.

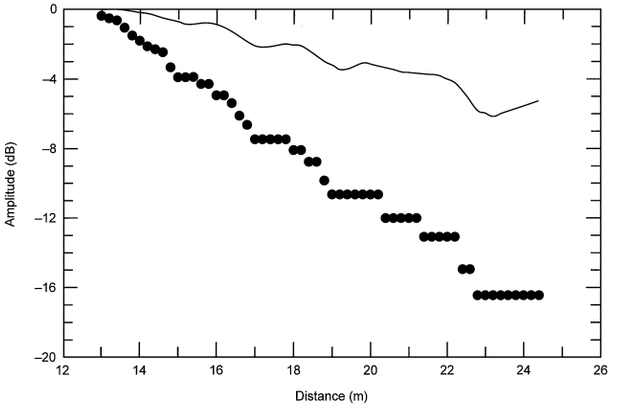

FIG. 11. Time-domain amplitudes of the 60–70-MHz packet. The data points are the raw values, and the solid line is a smoothed version of the values corrected for $1/r^2$ geometric spreading loss. The stepped appearance of the uncorrected data results from amplitude quantization.

for a 34-cm layer of $\varepsilon_2 = 23$ above a substrate of $\varepsilon_3 = 10.6$, the TE_1 solution [left side of equation (1) $= 1.0 + i0.0$] for 30 MHz predicts $\theta = 43.1°$, which is the critical angle that causes refraction in the lower medium. A solution at 90° exists at all frequencies and is physically irrelevant. As frequency increases, the solutions move to higher angles, while new modes (TE_3, TE_5; TE and TM mode numbering is by twos) eventually set in at the critical angle, as seen best at 280 MHz. The solutions were computed to an accuracy of better than 0.01 in both real and imaginary parts.

There is no solution below 30 MHz unless a finite value of γ is used, so that 30 MHz is also the cutoff frequency. A Fourier analysis of the last trace recorded on the south-side profile (Figure 12) shows the spectral amplitude at this frequency to be very small. Therefore, what appear to be refractions at progressively lower frequencies in Figure 8 are actually the faster speed, lower frequencies propagating near cutoff within the TE_1 mode. Obviously, these frequencies must be matched by a refracting wave in the lower medium. Any higher, matching frequencies in the second layer are not permitted to refract by the requirement of phase continuity across the interface, so they may exist as head waves.

The TE_1 solutions at 30 and 65 MHz ($\theta = 50.5°$, Figure 12), give phase velocities equivalent to $\varepsilon = 10.6$ and 13.5, respectively; these values are close to the phase speed equivalent ε values of 10 and 15 that we measured from the profiles in Figure 8. Figure 12 also shows that by the antenna design frequency of 100 MHz, there is still only one mode allowed; a second, TE_3 mode will not start until about 170 MHz. By 280 MHz, three modes will be excited.

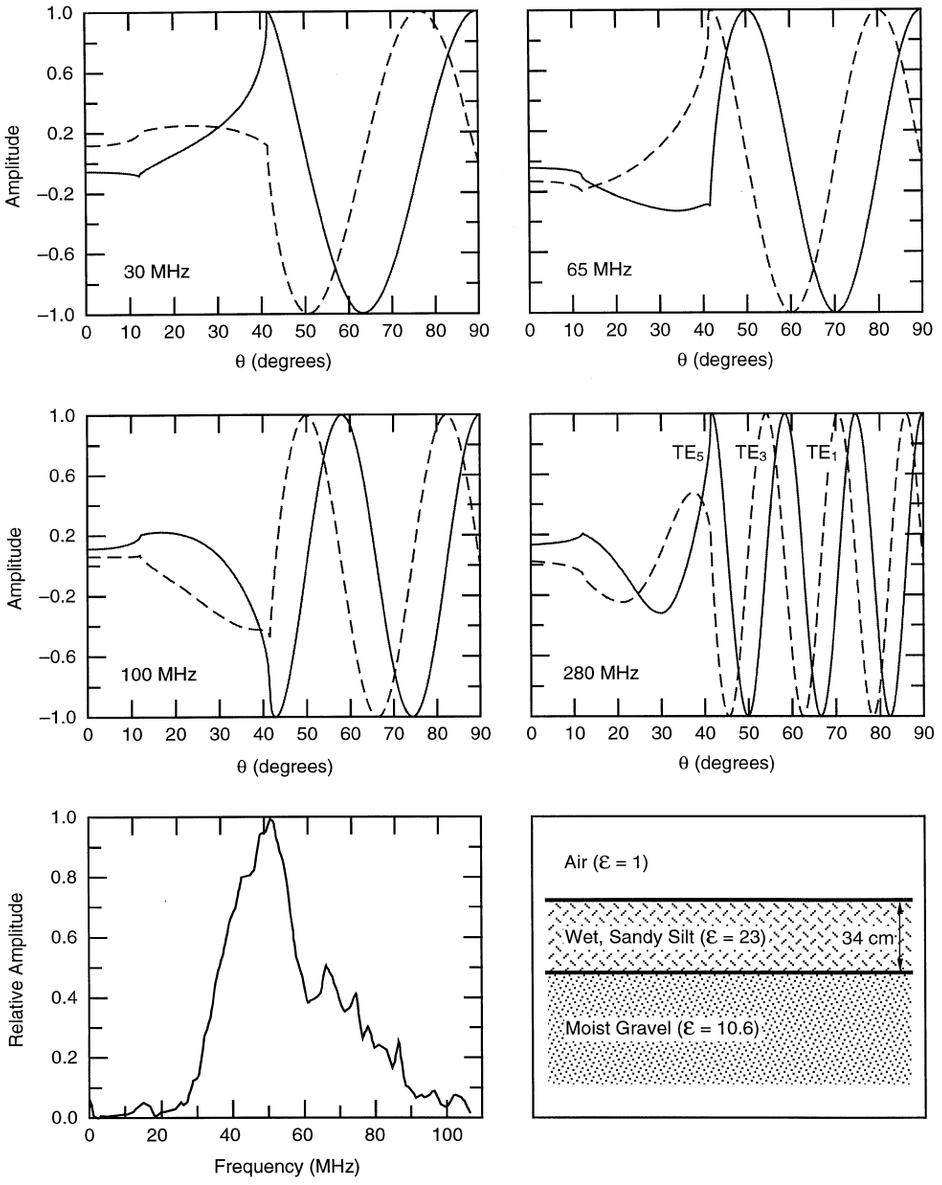

FIG. 12. TE_1 solutions to equation (1) at 30, 65, 100, and 280 MHz, and spectrum of the trace recorded at 35 m separation of the south offset profile (lower left).

Figure 13 shows theoretical phase and group velocities as a function of frequency, where the group velocity was determined numerically from the phase velocity by

$$v_{gr} = \frac{v_{ph}}{1 - \left(\frac{f}{v_{ph}}\right)\left(\frac{\partial v_{ph}}{\partial f}\right)}. \quad (4)$$

Near 30 MHz both speeds approach that of the refracting layer, to which the curves are normalized. A minimum group velocity is reached at about 150 MHz. Theoretically, the Airy phase of pulse propagation should occur at this minimum frequency, as it would for a reflective (Arcone, 1984), rather than a refractive, waveguide. However, there is no propagation at this frequency in Figure 8. The group velocity predicted at 65 MHz has an equivalent ε_2 of 24; the value from Figure 8 is about 30.

We explain the diagonal streaks in the 280-MHz reflection profile with a higher frequency analysis of the TE modes in Figure 12. The slopes of these profile events give $\varepsilon_2 = 16$–21. The thickness of this layer and the high value of ε permit three transverse electric modes to propagate at 280 MHz. The dominant, TE_1 mode propagates at a value of $\theta = 74.5^\circ$, which corresponds with $\varepsilon_2 = 21.1$. At this high frequency the theoretical group velocity is within a few percent of the phase velocity (Figure 13). The predicted refraction at 43° is not seen in the 280-MHz reflection profiles (as a scattered event) because it occurs as the TE_5 mode, which would be weakly excited.

Qualitative 2D, FDTD numerical modeling

We also performed 2D pseudospectral FDTD numerical modeling (Xiao et al., 1998) to simulate the waveguide propagation. We assigned resistivities of 2000 and 5000 ohm-m to the upper and lower layers, respectively. The propagation shown in Figure 14 for a 34-cm layer generally reproduces that seen in Figure 8. Lower frequency modes propagate fastest and die off at the front of the mode, and higher frequencies propagate at progressively slower speeds. In both the field and model synthetic data, a slight decrease in the slopes of the phase fronts toward the widest spacing can be seen upon close inspection of the profile. For comparison, a 51-cm model is also shown, and the results are distinctly different: the leading phase fronts are wider in time, and higher frequency shingling is more distinct at the trailing edge of each pulse. There are no apparent back-reflected modes in the model, so we interpret them in the field data to be waveguide reflections. The 2D nature of the modeling prevents us from making a fair analysis of the causes of amplitude attenuation.

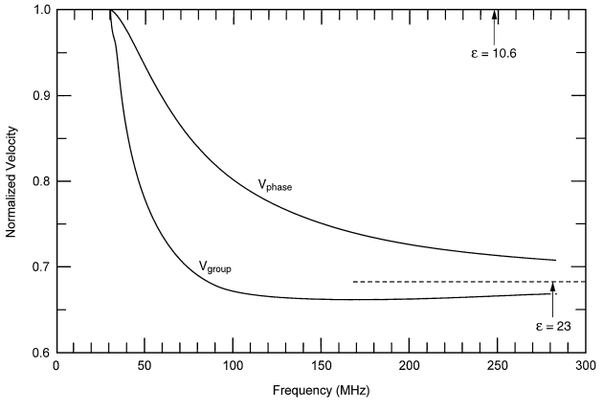

FIG. 13. Phase and group velocities of the waveguide as a function of frequency. The speeds are normalized to the refracting layer speed.

Attenuation processes

The average rates for the three half-cycles in Figure 10 far exceed what would be predicted by a resistivity of 1000 to 2000 ohm-m and are inconsistent with the 0.4-dB/m rate determined for the 60–70-MHz packet. Therefore, the rates in Figure 10 for the 30–50-MHz portion must be strongly affected by the dispersive process within the propagation. In contrast, the rates measured in Figure 11 for the 60–70-MHz packet are for a group of waves that maintained their dominant frequency, so we consider this rate to be more reliable for the medium. However, we interpret the erratic amplitudes of Figure 10 to indicate scattering, most likely from interface roughnesses. Similar amplitude behavior is shown by Laster et al. (1967) in an analog model study of seismic refraction along an uneven interface. Our interpretation of the presence of scattering is also consistent with

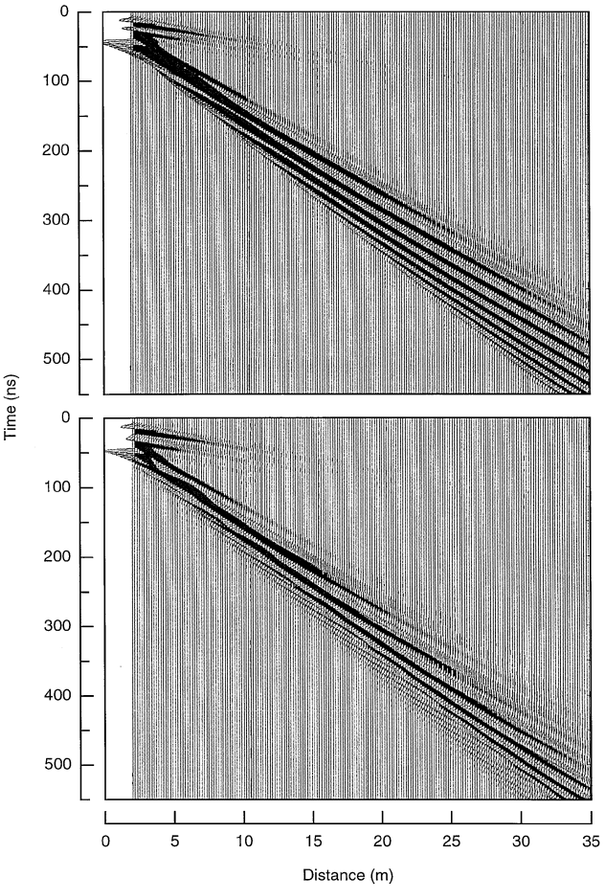

FIG. 14. Simulated waveguide propagation for our model 34-cm waveguide (top), and modeling of a 51-cm waveguide (bottom) for comparison. A 65-MHz DF-simulated GPR pulse is the excitation. Automatic gain control has been applied to make all events visible.

the appearance of the backscattered packets in Figure 8 and the sloping events of the reflection profiles.

The dc conduction losses partially account for the 0.44-dB/m rate for the 60–70-MHz part of the energy. Losses caused by relaxation and single scattering are calculated to be minimal (see Appendix), while waveguide measurements on dry, silty sand samples from the waveguide layer show no magnetic losses. When conduction currents are considerably weaker than displacement currents, the attenuation rate β_{dc} is independent of frequency and is expressed as

$$\beta_{dc} = \frac{8.686}{2c\rho\varepsilon_0\sqrt{\varepsilon_2}}, \tag{5}$$

where $\varepsilon_0 = 8.854 \times 10^{-12}$ F/m. For the upper layer, $\varepsilon_2 = 23$; then the minimal value of $\rho = 885$ ohm-m gives $\beta_{dc} = 0.39$ dB/m from 30 to 100 MHz. Thus the lowest measured resistivity accounts for the 60–70-MHz loss rate. The highest value, 2700 ohm-m, gives $\beta_{dc} = 0.13$ dB/m.

Processing errors were not systematic. Our choice of measuring either peak cycle amplitudes (30–50 MHz) or the amplitude of the envelope (60–70 MHz) is virtually equivalent to measuring area under the waveform, and the same procedure was applied at all distance stations. The major source of error was most likely the impedance loading of the coupling between the receiver antenna and the ground surface. If we assume a simple square-root dependency of amplitude on ε, as generally occurs for wave impedances, then the estimated ε variation of 21 to 25 about a mean value of 23 would produce an error of about 5% in the amplitudes. Such an error could, at most, change the 60–70-MHz rate of 0.44 dB/m to either 0.36 or 0.51 dB/m and provide a maximum error of about 18% in the attenuation rate. Both of these values still reasonably agree with the 0.39-dB/m rate predicted by the minimum 885 ohm-m resistivity we measured for this layer.

There are, of course, other loss mechanisms that can contribute a few tenths of a decibel per meter. Calculations of single scattering loss based on the formulations of Smith and Evans (1972) for 8% volumetric clasts of $\varepsilon = 10$ embedded in a matrix of $\varepsilon = 23$ give about 0.01 dB/m at 65 MHz, even though 8% is large for this theory. Similarly, calculations based on the CRIM mixing formula give water relaxation loss rates less than 0.1 dB/m. Other possible relaxation losses exist, but the appearance of erratic amplitudes and backscattered modes strongly suggests that scattering was probably the only other significant loss mechanism.

CONCLUSIONS

The interpretation of electrical properties and structure from propagation within an electrically thin layer requires consideration of dispersive modal propagation rather than simple ray optics propagation. For the case of a refracting second layer, it appears possible to estimate the layer relative permittivities from the phase and group velocities of the low- and high-frequency parts of a single mode. The lowest 30-MHz phase velocity gave a permittivity value ($\varepsilon_3 = 10$) that corresponded with that of the lower layer, while the higher, 60–70-MHz group velocity gave a value ($\varepsilon_2 = 30$) above that of the upper layer ($\varepsilon_2 = 23$). Since theory predicts that this group velocity value should correspond with $\varepsilon_2 = 24$, it therefore seems that a better estimate might have been obtained if we had extended the profile to get a more accurate measure of the slope of the shingled phase fronts. The theory shows that our accuracy in measuring group velocity was about 12%.

The measurement of attenuation appears problematic. Irregularities in layer thickness may cause scattering, and attenuation of any particular frequency is also caused by the dispersion. We believe our standard deviation of 20% in thickness is responsible for the amplitude variability at 30 to 50 MHz. Our difficulty in verifying this stems from problems with assessing the contribution of the many loss processes that can exist, especially in a sediment with a large, coarse-grained fraction and highly variable mineralogy. Future 3D FDTD modeling may greatly help to differentiate dispersive from natural attenuation processes.

The high resistivity of the surface materials indicated by the Wenner data, along with the substantial water content indicated by the GPR data and sampling, suggest that the pore water had a low ion content and that the host material was relatively free of clays.

It appears that commercial-grade, resistively loaded dipoles have sufficent bandwidth to receive the lower frequencies, but that the higher frequencies may be limited by the loading of the ground impedance. We also conclude that a wide antenna separation is possible and must be used; we needed about 25 m to achieve the cutoff frequency of about 30 MHz, and it is obvious from the profiles that separations of probably 50 m were possible. The frequency spectrum appears to show this correct cutoff and could be used in the field as a guideline for analytic confirmation.

ACKNOWLEDGMENTS

This work was supported by the Directorate of Public Works, Environmental Resources Branch of the U.S. Army Alaska, Fort Richardson, Alaska, and by the Department of Defense, DA project 4A161102AT24. We would like to thank Allan Delaney, Eric Williams, Norbert Yankielun, and Beth Astley of ERDC/CRREL for their field and computational support. We gratefully acknowledge the helpful comments of John Hermance. The numerical code for the FDTD modeling was modified from Taflove and Hagness (2000).

REFERENCES

Annan, A. P., 1973, Radio interferometry depth sounding: Part I—Theoretical discussion: Geophysics, **38**, 557–580.

Annan, A. P., Cosway, S. W., and Sigurdsson, T. S., 1994. GPR for snow pack water content: 5th Internat. Conf. on Ground Penetrating Radar, Proceedings, 465–475.

Arcone, S. A., 1984, Field observations of electromagnetic pulse propagation in dielectric slabs: Geophysics, **49**, 1763–1773.

Arcone, S. A., Lawson, D. E., Delaney, A. J., Strasser, J. C., and Strasser, J. D., 1998, Ground-penetrating radar reflection profiling of ground water and bedrock in an area of discontinuous permafrost: Geophysics, **63**, 558–669.

Astley, B., Snyder, C. F., Lawson, D. E., Delaney, A. J., Arcone, S. A., Hunter, L. E., Bigl, S. R., and Staples, A., 1999, Stratigraphy, aquifer distribution and potential contaminant migration pathways based on ground resistivity and ground-penetrating rader analyses: Water Treatment Plant, Fort Richardson, Alaska: U.S. Army Alaska Directorate of Public Works, Fort Richardson, AK.

Budden, K. G., 1961, The wave-guide mode theory of wave propagation: Prentice-Hall, Inc.

Campbell, M. J., and Ulrichs, J., 1969, Electrical properties of rocks and their significance for lunar radar observations: J. Geophys. Res., **74**, 5867–5881.

Cumming, W. A., 1952, The dielectric permittivity of ice and snow at 9.35 centimeters: J. Appl. Phys., **23**, 768–773.

Ewing, M., Jardetzky, W. S., and Press, F., 1957, Elastic waves in layered media: McGraw-Hill Book Co.
Fisher, E., McMechan, G. A., and Annan, A. P., 1992, Acquisition and processing of wide-aperture ground-penetrating radar data: Geophysics, **57**, 495–504.
Grant, F. S., and West, G. F., 1965, Interpretation theory in applied geophysics: McGraw-Hill Book Co.
Heelan, P. A., 1953, On the theory of head waves: Geophysics, **18**, 871–893.
Hunter, L. E., Lawson, D. E., Bigl, S. R., Robinson, P. B., and Schlagel, J. D., 2000, Glacial geology and stratigraphy of Fort Richardson, Alaska: U.S. Army ERDC Cold Regions Research and Engineering Laboratory Technical Report **TR-00-3**.
Laster, S. J., Backus, M. M., and Schell, R., 1967, Analog model studies of the simple refraction problem, *in* Musgrave, A. W., Ed., Seismic refraction prospecting: Soc. Expl. Geophys, 15–66.
O'Brien, P. N. S., 1967, The use of amplitudes in seismic refraction survey, *in* Musgrave, A. W., Ed., Seismic refraction prospecting: Soc. Expl. Geophys, 85–118.
Shutko, A. M., and Reutov, E. M., 1982, Mixture formulas applied in estimation of dielectric and radiative characteristics of soils and ground at microwave frequencies: IEEE Trans. Geosci. Rem. Sens., **GE-20**, 29–32.
Smith, B. M. E., and Evans, S., 1972, Radio echo-sounding: Absorption and scattering by water inclusions and ice lenses: J. Glaciol., **11**, 133–146.
Taflove, A., and Hagness, S. C., 2000, Computational electromagnetics: Artech House.
Topp, G. C., Davis, J. L., and Annan, A. P., 1980, Electromagnetic determination of soil water content: Measurements in coaxial transmission lines: Water Resources Res., **16**, 574–582.
Winkler, G. R., 1992, Geologic map and summary geochronology of the Anchorage $1^\circ \times 3^\circ$ quadrangle, southern Alaska: U.S. Geol. Survey Misc. Investigations Map I-2283, scale 1:250 000.
Xiao, L., Liu, L., and Cormier, V. F., 1998. Two-dimensional finite-difference time-domain solution for Maxwell's equations using pseudo-spectral method: 7th Internat. Conf. on Ground Penetrating Radar, Proceedings, 585–589.

APPENDIX

DIELECTRIC PERMITTIVITIES OF CLASTIC MATERIALS

We measured the relative permittivities of large glacial erratics at Fort Richardson to better understand the high dielectric constants of the layers and the possibility of scattering. We assume that the sand grains and clasts found in our glacial sediments are mineralogically similar to the large granite, diorite, greywacke, and volcanic boulders found throughout the area. Glacial silt, on the other hand, is usually mostly quartz. Many of these boulders are flat-sided from glacial erosion, which allowed reflection profiling with the 1200-MHz antenna system (Figure A-1). We then determined ε_m from the time delays and rock thicknesses. At this frequency the real part of the dielectric permittivity of most rocks appears to be marginally different from those at 100 MHz for these rock types (Campbell and Ulrichs, 1969). The values for 14 rocks ranged between 7 and 14, and the average ε_m is about 9 ± 1. The error source is mainly in the accuracy of our measurement of thicknesses, which were on the order of 1 m, while round-trip time delays were usually about 20 ns. Our thickness accuracy was no better than 5 cm, which could also have been provided by the actual raypath distances between the slightly nonparallel faces.

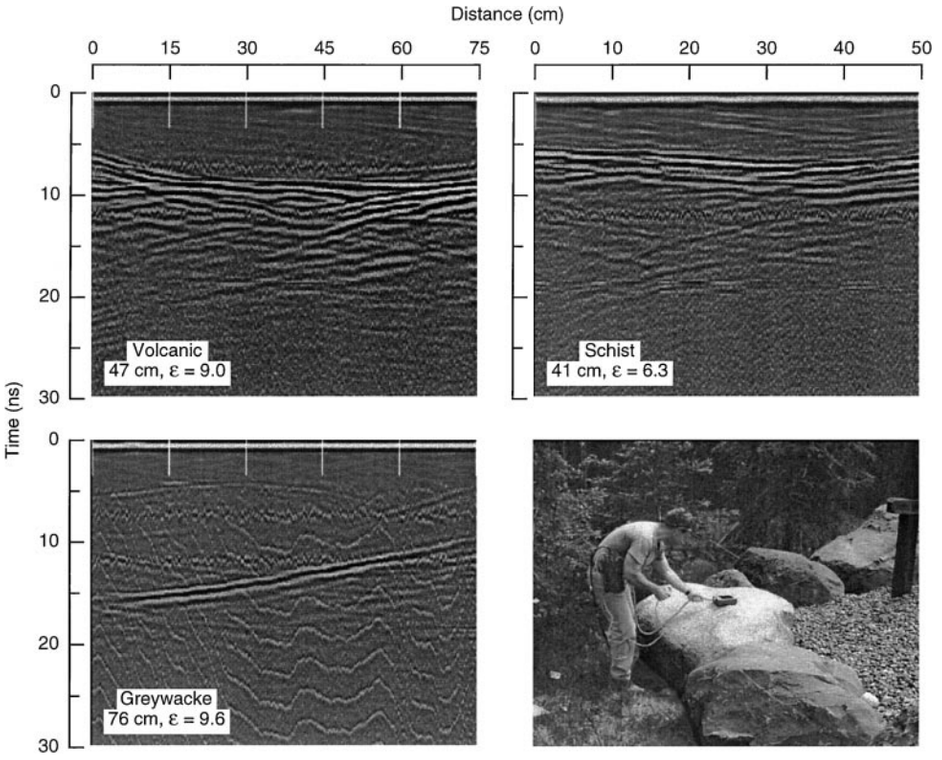

FIG. A-1. Sample 1200-MHz reflection profiles of boulders at Fort Richardson, and photograph of profile recording. The labels indicate maximum thickness and calculated value of ε. The erratic lines in the profile at lower left are caused by the system power supply.

We applied the results to the CRIM formula (Annan et al., 1994; Shutko and Reutov, 1982) for the composite refractive index n, such that

$$n = \theta_m \sqrt{\varepsilon_m} + \theta_a \sqrt{\varepsilon_a} + \theta_w \sqrt{\varepsilon_w^*}, \qquad \text{(A-1)}$$

where θ_m, θ_a, and θ_w are the volumetric mineral, air and water contents, respectively, and ε_m, ε_a, and ε_w^* are the real parts of their relative dielectric permittivities. We assume that $\varepsilon_w = 84$ (at a summer soil temperature near 5°C) is the relative permittivity below 1000 MHz. Equation (A-1) provides real index values which agree very well with laboratory data for a variety of soils (Topp et al., 1980) over a wide range of moisture contents and for snow (Cumming, 1952) over a wide range of densities. Other, more physically based approaches (Shutko and Reutov, 1982) give comparable results for simple, two-component sediments.

For the upper layer, our calculated values of $\theta_m = 0.53$, $\theta_a = 0.18$, and $\theta_w = 0.29$ give $n = 4.44$ and $\varepsilon_2 = 19.7$. For the refracting layer, $\theta_m = 0.81$, $\theta_a = 0.11$, and $\theta_w = 0.08$ give $n = 3.27$ and $\varepsilon_3 = 10.7$. Thus, the gravel value is well predicted, and the waveguide layer value is reasonably close. The discrepancy could well be explained by a low estimate of dry density (0.53) for this well-mixed variety of grain sizes that varied from 10 cm diameter to silt (4–75 μm).